ACS OMEGA

Open Access

http://pubs.acs.org/journal/acsodf

Article

Investigating the Reactive Reinforcement Ability of Maleic Anhydride-Modified Cellulose Nanocrystals via In-Situ Emulsion Polymerization

Radheesh Sharma Meda, Somya Jain, Shiva Singh, Dakuri Ramakanth, Shakshi Bhardwaj, Yoshikuni Teramoto, Prasenjit Mondal, and Pradip K. Maji*

Cite This: *ACS Omega* 2024, 9, 33386−33396

Read Online

ACCESS | Metrics & More | Article Recommendations | Supporting Information

ABSTRACT: CNC-based nanocomposites have gained substantial interest because of their enhanced thermomechanical properties for high-end engineering applications. The chemical modification of CNCs expands their applicability, making them suitable for use in hydrophobic polymer matrices. The current study investigates the reactive reinforcing ability of maleic anhydride-modified cellulose nanocrystals during the in situ polymerization of a vinyl monomer, i.e., styrene. Highly crystalline nanocellulose (CNCBG) was isolated from *Lagenaria siceraria* (Bottle gourd) peels via Hydrochloric acid, which was further modified to synthesize maleic anhydride-modified cellulose nanocrystals (MACNCBG) and characterized employing various techniques. MACNCBG exhibited higher suspension stability than CNCBG due to the introduction of carboxyl groups. Furthermore, polystyrene-based nanocomposites of 3 and 5 wt % filler loading were prepared, respectively. While PSMACNCBG (5 wt %) displayed a premature failure, PSMACNCBG (3 wt %) demonstrated enhanced mechanical properties compared to PSCNCBG (3 wt %) and PS. At the same filler loading, MACNCBG demonstrated a more remarkable reinforcing ability than CNCBG, owing to its reactive tendency. The appearance of a new peak between 3000−2800 cm^{-1} corresponds to the C−H stretching of the formed C−C bond (between C═C of MACNCBG and benzal carbon of PS) in the FTIR spectra, confirming the reactive nature of MACNCBG.

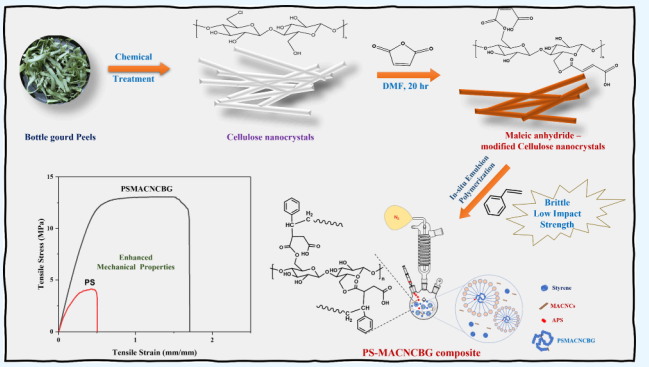

1. INTRODUCTION

Researchers have significantly focused on polymer nanocomposites due to their remarkable mechanical, dynamic-mechanical, and thermal properties.[1] Incorporating organic and inorganic fillers into the polymer matrix[2−7] not only results in cost reduction for the final product but also broadens its applications across various industries such as aerospace, automotive, biomedical, and construction. Additionally, various processing methods, including melt compounding, solution blending, in situ polymerization, etc., have been commonly employed to integrate fillers into the polymer matrix and create hybrid composites.[8−11] The current literature extensively explores the effects of organic and inorganic fillers on the mechanical properties of polymer composites, including cellulose, lignin, carbon nanotubes, alumina, and silica (SiO_2)-based composites.[2,12]

The most crucial step in developing composites is achieving compatibility between the selected fillers and polymers in terms of adhesion, ease of integration, and distribution of the filler within the polymer matrix.[11,13] Most fillers in present applications possess hydrophilic surface properties, rendering them incompatible with nonpolar or hydrophobic polymers. Surface compatibilization techniques are employed to overcome this inherent challenge, facilitating the homogeneous dispersion of fillers within the polymer matrix and the attainment of desired material characteristics.[11,14] One of the most favored approaches for surface compatibilization of filler with polymer matrix is chemical modification utilizing either reactive or nonreactive modifying agents.[5,15] Surface functionalized fillers can react chemically and exhibit weak aggregation and homogeneous behavior with the polymer matrix.

Natural components, including lignin, cellulose, and tannins, are increasingly preferred in the manufacturing of polymer composites instead of carbon black and mineral fillers. Cellulose is a biodegradable, renewable, nontoxic, and lightweight biopolymer widely distributed in nature. It

Received: October 8, 2023
Revised: February 5, 2024
Accepted: May 27, 2024
Published: July 26, 2024

provides the structural foundation for exceptional plant cells by providing mechanical qualities.[11,16−20] In crystalline and amorphous domains, cellulose is the repeating unit of D-anhydro glucopyranose (AGU) joined together by β-1,4-glycosidic linkages. The cellulose might be nanocrystalline or microcrystalline depending on its size. Nanocellulose (NC) refers to cellulose fibers or crystals with at least one dimension within the nano range. They commonly exist in the form of nanocrystals, rods, whiskers, or nanofibers.[17,21−23]

Cellulose nanocrystals (CNCs) have emerged as a promising reinforcing filler in nanocomposites based on various polymer matrices, including acrylic latex, poly(vinyl alcohol), polyurethane, polyethylene, natural rubber, polyester, and thermoplastic starch.[24−28] By comparing the mechanical characteristics of CNC-reinforced composites to those of other commercially available reinforcing agents, cellulose nanocrystals have much potential as a reinforcing material. Even though there are several publications discussing cellulose reinforcement in various polymeric materials, improving phase compatibility remains a major challenge.[23,28]

The previously reported works of literature established that introducing maleic anhydride on cellulose nanofibers improved its dispersion and interactions with hydrophobic polymer matrix.[22,29] However, there is limited literature available regarding the utilization of modified CNCs during in situ polymerization. In this report, the extracted cellulose nanocrystals were modified using maleic anhydride to fabricate the polystyrene-based composite during the in situ emulsion polymerization of styrene. For the first time, we have established that these maleic anhydride-modified cellulose nanocrystals have reacted with polystyrene during polymerization as a reactive filler, enhancing the mechanical stability of polystyrene films.

2. EXPERIMENTAL SECTION

2.1. Chemicals and Materials. The waste *Lagenaria siceraria* (Bottle gourd) peels were obtained from the Malviya Bhawan Mess of IIT Roorkee, Saharanpur Campus. Ethanol (C_2H_5OH 99.9% purity) was acquired from Changshu Hongsheng Fine Chemical Co. Ltd. (China). Sodium chlorite ($NaClO_2$), sodium sulfite (Na_2SO_3), potassium hydroxide (KOH), Tween 20, sodium hydrogen carbonate ($NaHCO_3$), ammonium persulfate, and dimethylformamide were purchased from Himedia Pvt. Ltd., India. Toluene, glacial acetic acid (CH_3COOH), hydrochloric acid (HCl), *n*-hexane, and isopropyl alcohol were procured from Rankem, India. Styrene was obtained from the AVRA Synthesis Pvt. Ltd., India, and maleic anhydride from SRL Chemicals, India. The current study used AR-grade chemicals, and the double distilled water (DW) utilized was obtained from the laboratory distillation unit.

2.2. Isolation of CNCs through Hydrochloric Acid. One g of pure cellulose was extracted from *Lagenaria siceraria* peels following the procedure established from previous works of literature[16,17,30] and further chemically treated with 35 mL of 4 N HCl solution.[31,32] The mixture was constantly stirred for approximately 4 h 15 min at 75 °C, and the reaction mixture was doused with 350 mL of chilled water. After quenching, the acidic solution was left overnight to settle; the supernatant was decanted, and the remaining CNC suspension was subjected to dialysis against distilled water (DW). When the pH rose to 7 after 2−3 days, the suspension was deep-frozen and lyophilized to obtain cellulose nanocrystals (CNCBG).

2.3. Synthesis of Maleic Anhydride-Modified Cellulose Nanocrystals (MACNCBG). The freeze-dried CNCBG (3 g) was added into 60 mL DMF & dispersed under constant stirring for 20 min. Following the dispersion of CNCBG, 30 g of MA was dissolved in the solution, and the modification was carried out at 120 °C for 20 h. After the conversion, the reaction was quenched with 300 mL ethanol, and the mixture was kept under stirring for 2 h before centrifugation, then diluted the sediment collected after centrifugation at 9000 rpm with the REMI; R-24, India, for 10 min with ethanol to remove unreacted MA and repeated the centrifugation-dilution process until there was no more change in the color of the mixture.[33] The color of the mix before centrifugation was black, containing unreacted MA, DMF, MACNCBG & ethanol. The centrifugation-dilution process altered it to brown at the end, containing MACNCBG and ethanol. The obtained MACNCBG was dispersed in DW & kept in deep freeze at −40 °C for a day and freeze-dried for 2 days. The freeze-dried MACNCBG was collected for further analysis with a yield of ∼90%.

2.4. Preparation of PS, PSCNCBG, and PSMACNCBG Nanocomposites. Polystyrene-based composites were synthesized using emulsion polymerization from pure styrene (free from inhibitor). The detailed schematic of inhibitor removal is illustrated in Figure S1. The reaction was performed in a three-neck round-bottom flask with 100 mL of DW, 5 g of Tween 20 as an emulsifier, and 16 mg of sodium bicarbonate as a buffer at 400 rpm. After a uniform mixture was prepared, the beaker was exposed to continuous heating at 75 °C on a magnetic stirrer. The filler of 3 wt % CNCBG was dispersed in the mix (Tween 20 + $NaHCO_3$ + water) before the addition of styrene to produce a PSCNCBG composite. After a few minutes of stabilization, an inert environment was created by flushing nitrogen gas (4−5 times). Then, 10 g of pure styrene monomer was added gradually into the reaction with the help of a glass syringe. 0.35 g of the initiator, ammonium persulfate, was added to 10 mL of DW, and a few drops (∼2 to 3 mL) were added eventually to the reaction mixture. After 20−22 h, the reaction was turned off and the solution was poured into a separate beaker. Approximately 50−100 mL of *n*-hexane was added, and the mixture was kept steady until the layers separated into polymerized styrene and unreacted styrene dissolved in the *n*-hexane layer. The upper layer of *n*-hexane was decanted afterward. Then, acidified propanol (1 mL of 11.4 N HCl dropped onto 100 mL of propanol) was used for coagulation purposes.[34] The emulsion was stirred and then kept steady until the coagulated layer formed at the topmost layer, occupying almost half of the beaker. The Tween 20 and buffers were removed during washing. The coagulated sample was transferred onto a glass Petri plate and left to dry in a vacuum oven for 24 h. A similar procedure was repeated with (3, 5 wt %) MACNCBG to produce PSMACNCBG composites. Scheme S1 illustrates the in-situ emulsion polymerization reaction process.

2.5. Film Preparation. The PS, PSCNCBG, and PSMACNCBG films were prepared using the solvent−casting procedure. One g of (PS, PSCNCBG (3 wt %), PSMACNCBG (3 wt %)) the sample was slowly added to 30 mL of THF and was allowed to stir at room temperature until the complete dissolution of PS, dispersion of PSCNCBG (3 wt %), and PSMACNCBG (3 wt %, 5 wt %). The solutions

https://doi.org/10.1021/acsomega.3c07849
ACS Omega 2024, 9, 33386−33396

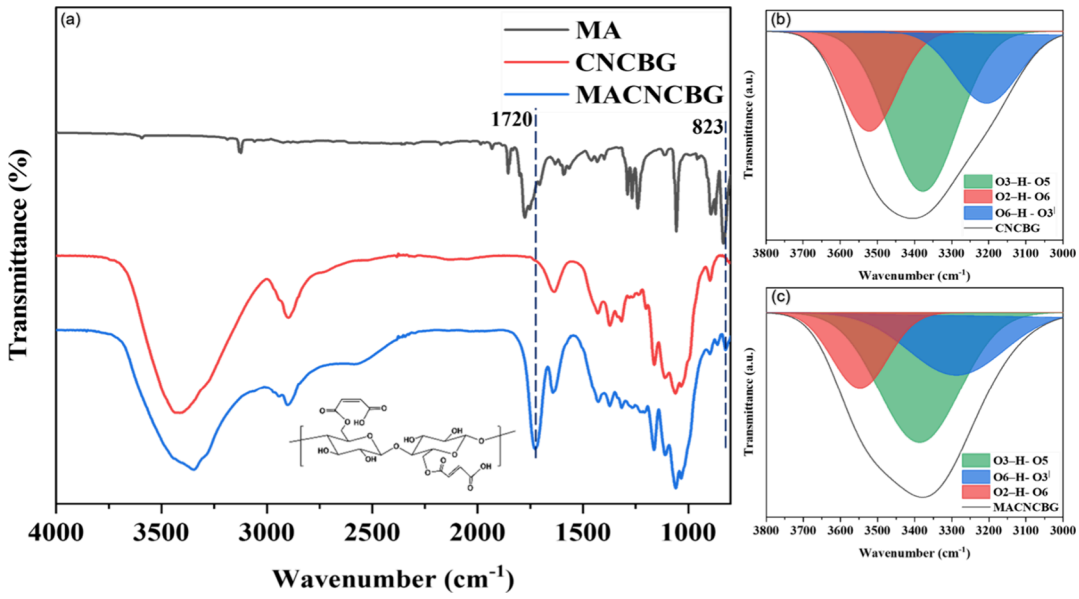

Figure 1. (a) FTIR spectra of MA, CNCBG, and MACNCBG, deconvoluted hydrogen bonding spectra of (b) CNCBG and (c) MACNCBG.

were cast in a glass Petri plate and dried at 35−40 °C for ∼4 h. The films were removed and cut into rectangular strips for further analysis.

3. CHARACTERIZATION

3.1. Fourier Transform Infrared Spectroscopy Analysis. The Infrared spectrum of the sample was recorded using Fourier Transform Infrared Spectroscopy (FTIR) in transmission mode with KBr pellets on a PerkinElmer FTIR spectrometer (USA). Operating at a resolution of 4 cm^{-1} per scan, the spectra were acquired over the 4000−520 cm^{-1} range for all instances. To comprehend the structural changes involved during the chemical modification of nanocellulose, the O−H stretching vibration was further analyzed by deconvoluting the symmetric spectra in the range 3800−3000 cm^{-1} under Gaussian fit using Origin 2021 Pro software. Similarly, to confirm the chemical interaction between the filler and matrix in the prepared composites, the C−H stretching vibration was examined under the spectrum range of 2900−2800 cm^{-1} by deconvoluting using Lorentz fit, which is used for asymmetric spectral lines.

3.2. ^{13}C Solid−State Nuclear Magnetic Resonance (ss−NMR). The carbon skeleton of the synthesized MACNCBG was verified through ^{13}C ss−NMR using *Jeol* 500. Samples (fine powder) were tightly crammed into a 4-mm O.D. zirconia rotor, spun at 8 kHz in nitrogen, and placed in an inert atmosphere. NMR spectra were acquired with 512 scans for each specimen and a pulse width of 0.4 s.

3.3. X-ray Diffraction (XRD). The crystal structure of CNCBG & MACNCBG was examined using X-ray diffraction (Rigaku Ultima IV model, from Japan). The X−ray source was a Copper K−alpha sealed tube producing a beam of electrons with a wavelength of 1.5405 Å with a 40 kV and 30 mA power source.

At a scan rate of 4°/min, the diffraction curves in the angular range (2θ scale) of 5−55° were obtained. The crystallinity index was evaluated by using the following methods: Segal Method and Area Method (Peak Deconvolution and amorphous Subtraction), which are governed by eqs 1 and 2. The former method was governed by the intensities of the crystalline and amorphous peaks, whereas the latter was governed by the area under the crystalline peaks.

$$\text{Crystallinity Index (C. I.)} = \frac{I_{200} - I_{AM}}{I_{200}} \times 100 \quad (1)$$

where I_{002} represents the maximum diffraction intensity (2θ = 22°) of the crystalline regions and I_{AM} (2θ = 18°) for the intensity of the amorphous peak.[35]

$$\text{C. I.} = \frac{A_c}{A_c + A_a} \times 100 \quad (2)$$

where A_c is the area under the crystalline peaks, and A_a represents the area of the amorphous peaks.[35]

In the case of the peak deconvolution method, the crystalline peaks at (101), (002), and (040) are deconvoluted using a Gaussian curve fitting in Origin Pro 2021 to calculate A_c. For the amorphous subtraction method, the amorphous spectrum (2θ = 18°) is subtracted from the original data to obtain A_c where no residual spectra contain a negative value. The total area of baseline-corrected spectra was evaluated ($A_c + A_a$).

3.4. X-ray Photoelectron Spectroscopy (XPS). To examine the surface chemical composition of the nanocomposite, X-ray photoelectron spectroscopy (XPS) was performed utilizing a PHI-5000-Versa Probe III photoelectron spectrometer (ULVAC-PHI INC, USA). The analyzer pass energies were 55 eV for the individual element spectra and 280 eV for the survey scan, using Al Kα as the radiation source. C_{1s} peak at 285.0 eV was utilized to calibrate the binding energy.

3.5. Field Emission Scanning Electron Microscopy Analysis (FESEM). Field emission scanning electron microscope (FESEM, MIRA3 TESCAN, USA) was employed to gauge the morphology of the sample surface by scanning a focused electron beam (accelerating voltage in between 5 and 10 kV) over the nanoparticles' surface to obtain a high-resolution image. The sample was prepared by drop−casting a significantly diluted (with a concentration of 0.001%) stirred solution of CNCBG and MACNCBG on a different glass slit, followed by oven drying at 50 °C to eliminate the moisture

https://doi.org/10.1021/acsomega.3c07849
ACS Omega 2024, 9, 33386−33396

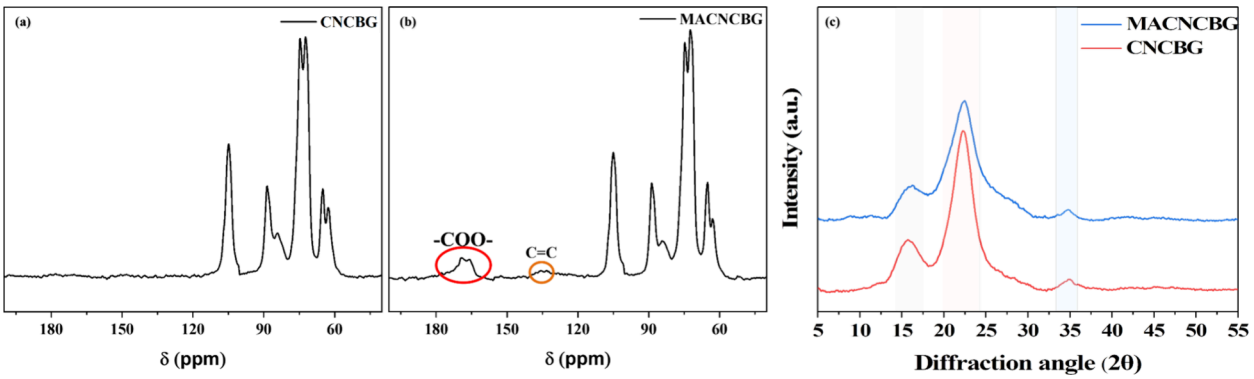

Figure 2. ^{13}C ss NMR of (a) CNCBG, (b) MACNCBG, and (c) XRD of CNCBG and MACNCBG.

content. The particle size distribution analysis was carried out using ImageJ software.

3.6. Zeta Potential (ζ)/Dynamic Light Scattering (DLS). Zeta Potential and Dynamic Light Scattering were used to examine the charge induced on the particles after hydrolysis and the particle size distribution of the CNCBG & MACNCBG suspension. Zeta Potential (ζ) magnitude was discussed along with the assistance of dynamic light scattering (Brookhaven instruments) in phase analysis light scattering (PALS) mode. Zeta potential (ζ) is computed from the suspension's electrophoretic mobility {(μm/s) /(V/cm)} with the Smoluchowski model.

3.7. Thermal Analysis. Thermal stability and degradation of CNCBG and MACNCBG were appraised using a thermogravimetric analyzer (TGA 55, TA Instruments, USA). Each specimen is heated from 27 to 600 °C at a 10 °C/min temperature increment rate in an N_2 environment at a 10 mL/min flow rate.

3.8. Mechanical Properties. To evaluate the ultimate tensile strength of the composite films, the sample was cut into rectangular strips of the following dimensions: 10 cm × 1 cm (length × width) and tested using a Universal Testing Machine (UTM, INSTRON, USA) using ASTM standards (D638). The film was clamped vertically, and the strain was set at 5 mm/min up to the breaking point and was carried out at room temperature. The thickness of the films was 0.0108 ± 0.006 cm.

4. RESULTS AND DISCUSSION

4.1. Filler Characterization Results and Discussion. *4.1.1. FTIR Spectroscopy.* The FTIR spectra of CNCBG & MACNCBG were analyzed to confirm the successful isolation of nanocrystals via hydrochloric acid and grafting of maleic–anhydride onto CNCBG, as shown in Figure 1a. A strong appearance of intense change in transmittance at 1720 cm^{-1} in MACNCBG corresponds to the carbonyl of the carboxyl/ester groups, establishing the formation of ester linkage on the surface of CNCBG. Also, the peak is ascribed to the esterification of alcohols and the formation of the ester linkage. The cyclic maleic anhydride carbonyl stretching is at a higher wavenumber 1785–1790 cm^{-1} and the ring opening led to the formation of acid/ester linkages, which have a stretching frequency at a lower wavenumber (1715–1720 cm^{-1}). In addition, the intense peak at 823 cm^{-1} is attributed to the out-of-plane deformation of carboxyl groups of MA. These observations established the successful grafting of maleic anhydride onto the CNCBG surface, and the relative grafting amount was evaluated to be 26.8%.[36] A detailed analysis of the chemical structural changes and the comprehensive analysis of the inter- and intramolecular hydrogen bonding were discussed in Supporting Information Section S2, and deconvoluted spectra are shown in Figure 1b,c.

4.1.2. ^{13}C ssNMR. The NMR of CNCBG is shown in Figure 2a, which is similar to a typical nanocellulose extracted from other sources.[17,37] The peaks between 60–110 ppm correspond with the cellulose I structure. The sharp peak at 105.4 ppm belongs to the anomeric carbon (C1), whereas the peaks between 71–75 ppm correspond to the C2/C3 and C5 of cellulose, respectively. Crystalline cellulose peaks are attributed to the C4 at 87.6 ppm and C6 at 64.5 ppm.[38] The amorphous region was associated with 84 ppm of C4.[35] The relatively low intensity signal at 84 ppm indicates the removal of amorphous regions via acid hydrolysis (HCl). No traces of hemicellulose or other components were found in the CNCBG due to the absence of these signals at 173, 56, and 21 ppm, which are related to the carboxyl groups in hemicellulose, methoxy groups, and methyl groups present in lignin.[39,40]

Similarly, ^{13}C NMR of MACNCBG is shown in Figure 2b with typical cellulose signals alongside an appearance of two new peaks, i.e., between 150 and 140 ppm, indicating C=C and around 180 pm corresponding to the carbonyl groups of ester/acid, which was in validation with the reported literature.[37,41] The relative grafting of MA on CNCBG was 28.4% and evaluated using the following eq 3

$$\text{NMR\% grafting yield} = \frac{S_0(3`)}{S_0(3`) + S_0(1)} \times 100 \quad (3)$$

where $S_0(3)$ corresponds to the area of carbonyl carbon (COO at 180 ppm) and $S_0(1)$ corresponds to the area of anomeric carbon (C1 at 105.4 ppm).[42]

4.1.3. X-ray Diffraction. The mechanical strength, thermal properties, and cellulose reinforcing capability depend on its crystalline characteristics, which were established through XRD. The degree of crystallinity also depends on the extreme hydrolysis conditions, as various reported approaches for hydrolysis may result in significant changes in the crystal structure. X-ray diffractograms of both CNCBG and MACNCBG are shown in Figure 2c.

The cellulose XRD diffraction patterns were recorded at 2θ = 16.45°, 22.55°, and 35.46°, which are characteristic peaks for the cellulose-I type structure corresponding to the lattice planes (110), (200), and (004).[16,17,35,43] The prominent crystalline peak was observed at 22.55°, confirming the presence of crystalline cellulose. The Segal method calculated

https://doi.org/10.1021/acsomega.3c07849
ACS Omega 2024, 9, 33386–33396

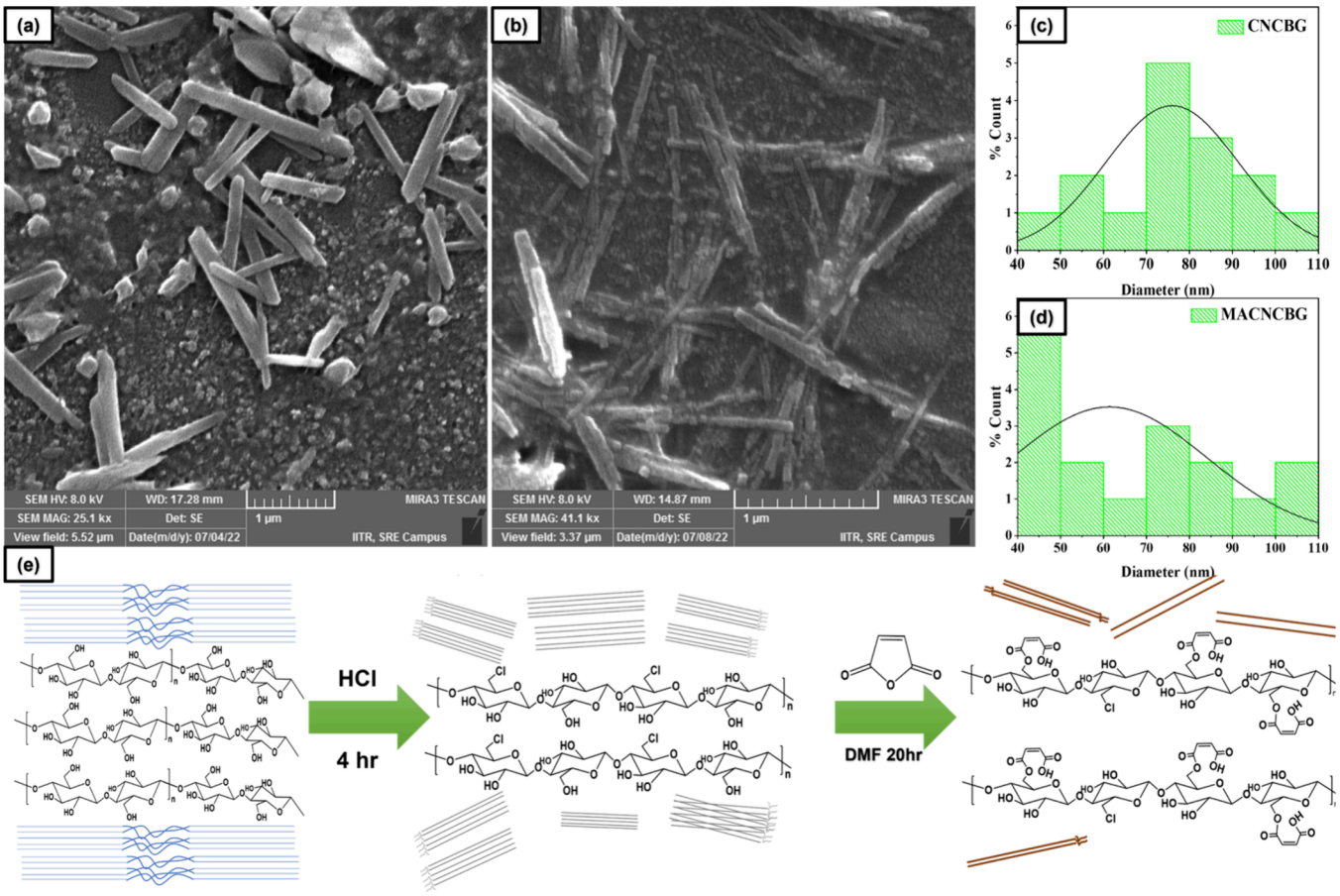

Figure 3. FESEM micrographs of (a) CNCBG, (b) MACNCBG and the particle size distribution, (c) CNCBG, and (d) MACNCBG, respectively, and (e) the plausible reaction pathway from acid hydrolysis until the maleic anhydride modification.

an 86% crystallinity index (C.I.) for the isolated CNCBG. This showed a significant increment in the crystallinity of cellulose after acid hydrolysis with HCl.[31,44]

However, the value of the crystallinity index for maleic anhydride-modified cellulose nanocrystals (MACNCBG) was lower than the CNCBG. Through the Segal method, 80% C.I. was calculated for MACNCBG. This led to the conclusion that the packing of cellulose chains and, hence, crystallinity was slightly destructed after the grafting of maleic anhydride as a pendant group during modification.[41,45] These variations were also supported by the other analysis methods of crystallinity, which are mentioned in Table S1, i.e., the amorphous subtraction and deconvolution method, as shown in Figure S2.

4.1.4. Morphological Analysis (FESEM). The morphology of CNCBG and MACNCBG was examined using FESEM, and micrographs are shown in Figure 3a,b. CNCBG and MACNCBG revealed a rod-like morphology with a higher aspect ratio (Length/Diameter), and the particle size distribution is displayed in Figure 3c,d. The utilization of HCl was the governing factor of the CNCBG morphology, with the crystal length ranging up to a few hundred nanometers, implying the withstanding of crystalline cellulose during acid hydrolysis.[31,44] H_2SO_4 dissolves disordered regions and relatively attacks the ordered areas, resulting in low yield and smaller dimensional nanocrystals.[16] Figure 3e illustrates the plausible reaction, implying chemical and structural changes. The average diameter of CNCBG and MACNCBG are 75 ± 0.8 and 54 ± 0.3 nm. The diameter was reduced by successfully grafting maleic anhydride onto the nanocrystals. Although the modification enhances the hydrogen bonding between the chains, from FTIR deconvolution, it is evident that the potential binding energy of intermolecular hydrogen bonding decreased from CNCBG to MACNCBG, resulting in narrower crystals. The higher-dimensional crystals improve the mechanical properties while incorporating in a polymer matrix.

4.1.5. Zeta Potential and Dynamic Light Scattering. The Zeta potential of CNCBG is −17.20 mV, which can be attributed to HCl hydrolysis. Unlike H_2SO_4, there is no dominant development of electrostatic repulsion over the attraction between the particles. CNCs extracted via H_2SO_4 have the substituted charged functional group $-OSO_3^-$, creating solid charge repulsion. However, with HCl, the −OH groups are replaced by an uncharged Cl atom with lone pairs. The low zeta potential value indicates weak repulsive forces, eventually leading to agglomeration of the nanocrystals and validating with the published literature using hydrochloric acid hydrolysis.[31,44] The aggregation of CNCBG led to a higher hydrodynamic diameter and was evaluated as 570 nm from DLS. The colloidal stability has been compromised despite producing highly crystalline nanocellulose through HCl. However, modification with maleic anhydride substantially improved the stability. The zeta potential of MACNCBG is −32.46 mV due to the substitution of carboxyl groups ($-COO^-$), generating a highly negative electrostatic barrier between the crystals. The modified MACNCBG crystals led to a lower average hydrodynamic diameter of 222.31 nm.

4.1.6. Thermal Analysis. The thermal stability of CNCBG and MACNCB was analyzed using thermogravimetric analysis

https://doi.org/10.1021/acsomega.3c07849
ACS Omega 2024, 9, 33386−33396

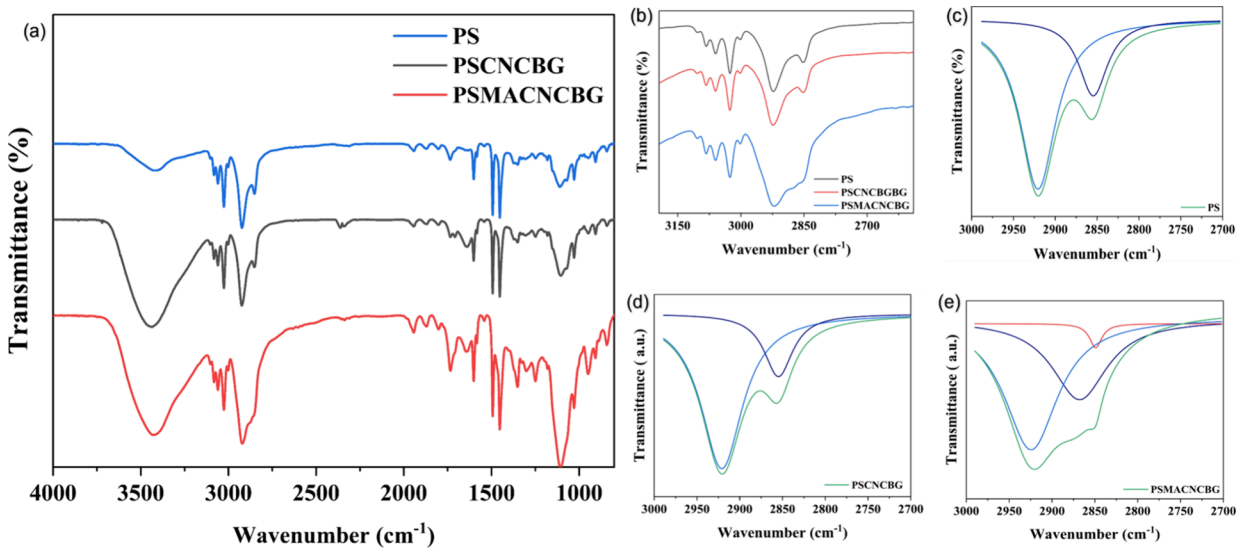

Figure 4. (a) FTIR spectra of PS, PSCNCBG, PSMACNCBG, (b) deconvolution region, and the deconvoluted C−H stretching vibration in 3000−2800 cm^{-1} of (c) PS, (d) PSCNCBG, and (e) PSMACNCBG.

Table 1. Deconvoluted C−H Stretching Vibration in 3000−2800 cm^{-1} To Comprehend the Chemical Changes Between Filler and Matrix

sample name	wavenumber (cm^{-1})	chemical bond	~content (%)
PS	2920	C−H of CH_2 in−$[CH_2 - CH(-Ph)]_n$−	72.9
	2854	C−H of−$[CH_2 - CH(-Ph)]_n$−	27.1
PSCNCBG	2920	C−H of CH_2 in−$[CH_2 - CH(-Ph)]_n$− &C−H of CH_2 in CNCBG	76.9
	2854	C−H of−$[CH_2 - CH(-Ph)]_n$−	23.1
PSMACNCBG	2924	C−H of CH_2 in−$[CH_2 - CH(-Ph)]_n$−	59.9
	2876	C−H of−$[CH_2 - CH(-Ph)]_n$−	36.8
	2849	C−H of new C−C linkage between MACNCBG and PS	3.3

(TGA), and derivative thermogravimetric (DTA) curves are shown in Figure S3a,b. The initial weight loss of 4 wt % corresponds to the absorbed moisture content before 200 °C in CNCBG. The extracted CNCBG has exhibited a single-stage degradation profile, unlike the CNCs isolated through H_2SO_4, which display a multistage degradation profile. The isolated CNCBG via HCl showed a relatively higher onset temperature (250 °C) than CNCs extracted through H_2SO_4 as shown in Figure S3c,d. Unlike CNCs from H_2SO_4 with multiple degradation temperatures at 275 & 485 °C, CNCBG has only a single maximum degradation temperature (333 °C) with a maximum weight loss of 80 wt % in the region between 250−400 °C. This can be attributed to the absence of sulfate groups ($-O-SO_3^-$), which decreases pyrolysis activation energy for pyrolysis.[16,17]

However, MACNCBG displayed a multistage degradation profile with two peaks in the DTA curve at 155 and 322 °C. The initial weight loss (16 wt %) between 120−180 °C can be attributed to tightly bound moisture to the carboxyl groups and the decarboxylation of substituted maleic anhydride in the disordered regions,[46,47] which can be corroborated with the decrement of C.I. of MACNCBG from the XRD analysis. The DTA curve reached a steady state between 230−240 °C before the accelerated decomposition began at 245 °C. The maximum weight loss (68 wt %) between 245−400 °C corresponds to the cleavage of glycosidic linkages and depolymerization of cellulose with a maximum degradation temperature of 320 °C. The single ultimate degradation of extracted CNCBG and synthesized MACNCBG indicates a narrow size distribution of nanocellulose and a controlled degree of substitution. Using traditional H_2SO_4 improves the suspension stability at the expense of thermal stability, differentiating between the ordered and amorphous regions, leading toward a wide distribution spread, which constrained the nanocrystals for thermal applications. With HCl, the nanocrystals are not distinguished into two areas of thermal degradation and exhibit a higher crystallinity index with a narrow distribution.[31,44] Somseemee et al. modified the CNCs with maleic anhydride, which was extracted from H_2SO_4, which displayed a two-stage degradation between 220−300 °C and 330−400 °C with two DTA peaks at 270 and 350 °C, which is in correspondence with the statements mentioned above.[41]

4.2. Nanocomposite Characterization. *4.2.1. FTIR Spectroscopy.* Scheme S1 illustrates the possible reaction process during the in situ polymerization of styrene alongside CNCBG & MACNCBG as reinforcers, resulting in the formation of PS, PSCNCBG, and PSMACNCBG. The successful polymerization of styrene was validated through the FTIR spectra of styrene and polystyrene, as shown in Figure S4. The complete disappearance of the peak at 1685 cm^{-1} corresponds to the stretching vibration of the C═C vinyl group in the styrene, validating the successful polymerization of PS. The detailed structural analysis was discussed in Supporting Information section S3.

Both the PSCNCBG (3 wt %) and PSMACNCBG (3 wt %) spectra displayed all the vibrations of PS alongside the appearance of distinguishing signals of cellulose (Figure 4a). A strong, broad, intense peak between 3800 and 3000 cm^{-1}

https://doi.org/10.1021/acsomega.3c07849
ACS Omega 2024, 9, 33386−33396

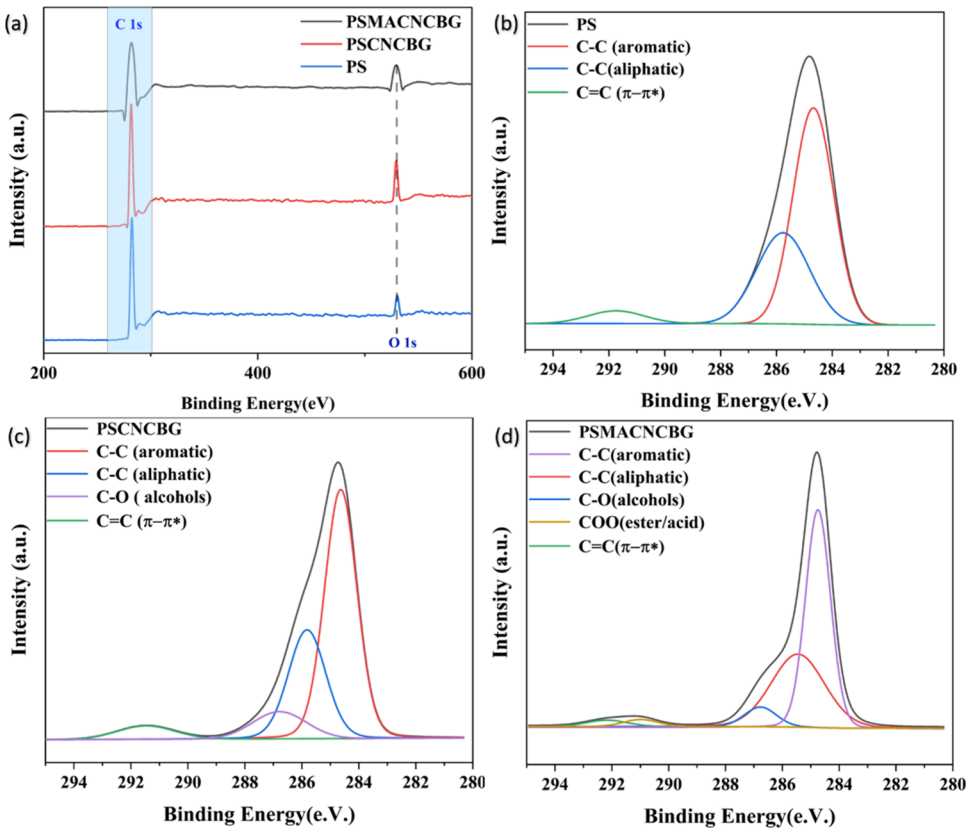

Figure 5. (a) XPS spectrum of CNCBG and MACNCBG, and deconvoluted C 1s ranges of (b) PS, (c) PSCNCBG, and (d) PSMACNCBG.

corresponds to the hydroxyl groups of the CNCs. The following bands in the regions 1330−1310 cm^{-1} and 1160−1050 cm^{-1} correspond to the stretching vibration of C−O and C−O−C linkages[11,30] of cellulose. The C−H deformation of the anomeric cellulosic carbon at 897 cm^{-1} indicated the successful incorporation of reinforcers in the PS.[33] There was also a broadening of the 3000−2800 cm^{-1} peak in the prepared nanocomposites, which can be noted in Figure 4b. To understand the reason behind this broadening, the area between 3000−2800 cm^{-1} was meticulously deconvoluted using Lorentzian fit and shown in Figure 4c−e. From the spectra of PS, it is evident that the peaks at 2920 and 2854 cm^{-1} correspond to the C−H stretching of methylene and the benzal group with 73 and 27% bond areas, respectively. The C−H stretching vibration of the cellulose pyranose ring also falls under this particular spectral band. PSCNCBG exhibited an increment of 3% for the spectra at 2920 cm^{-1}, indicating the overlapping of C−H stretching vibrations of both PS and CNCBG, implying no chemical interaction between CNCBG and PS during the in situ polymerization. The rationalized values of the bonds are summarized in Table 1.

On the contrary, PSMACNCBG displayed a broadening peak signal at 2854 cm^{-1}, associated with the benzal group in PS. Such a similar broadening was reported by Samadi et al. for poly(styrene-*alt*-maleic anhydride).[48] On deconvoluting the spectra, a new peak appeared at 2876 cm^{-1}, and a shift in benzal carbon (C−H stretching) to 2849 cm^{-1} was observed. The hydrophobic MA modification of CNCBG introduced a C═C bond in MACNCBG, and during the in situ polymerization of styrene, the MACNCBG chemically interacted with the styrene monomer units. MACNCBG can be attached to either benzal or methylene carbon. The spectra deconvolution validates the plausible mechanism shown in Figure S5, with a shift in substituted benzal C−H stretching toward a higher wavenumber (2876 cm^{-1}), implying a new chemical bond formation.

The signal at 2920 cm^{-1} corresponds to the overlapped summation of C−H stretching of both CNCBG and PS. With the plausible mechanism, the appearance of a new peak at 2876 cm^{-1} corresponding to C−H stretching of the C−C bonds-(unsaturated C atoms of MA and benzal carbon of PS), which is between 3 and 4%, resulted from chemical bonding between MACNCBG and PS. Similarly, the sharp, intense change in transmittance at 1733 cm^{-1} corresponds to the carboxyl groups of the ester/acid. The spectra of PSMACNCBG exhibited the characteristic bands of PS and MACNCBG and a significant transformation in C−H stretching vibrations, validating the successful utilization of MACNCBG as a reactive filler. The previously published articles reported a similar quantification of maleic anhydride grafting onto a polymer matrix.[36] The FTIR of PSMACNCBG (5 wt %) is shown in Figure S6a, and the absence of peak boarding between 2900−2800 cm^{-1} implies no chemical interaction.

4.2.2. XPS Analysis. The surface chemical composition of PS, PSCNCBG (3 wt %), and PSMACNCBG (3 wt %) was examined quantitively using XPS analysis and is shown in Figure 5a. The sharp, distinct peaks at 282 and 530 eV correspond to the C 1s and O 1s orbitals. The atomic weight percentages of C and O are tabulated in Table S2. It was evident with the increase in Oxygen content of both PSCNCBG and PSMACNCBG, implying the successful filler incorporation. The high-resolution deconvoluted C 1s spectra with three distinct peaks in PS, four in PSCNCBG, and five in PSMACNCBG are depicted in Figure 5b−d. The spectra

https://doi.org/10.1021/acsomega.3c07849
ACS Omega 2024, 9, 33386−33396

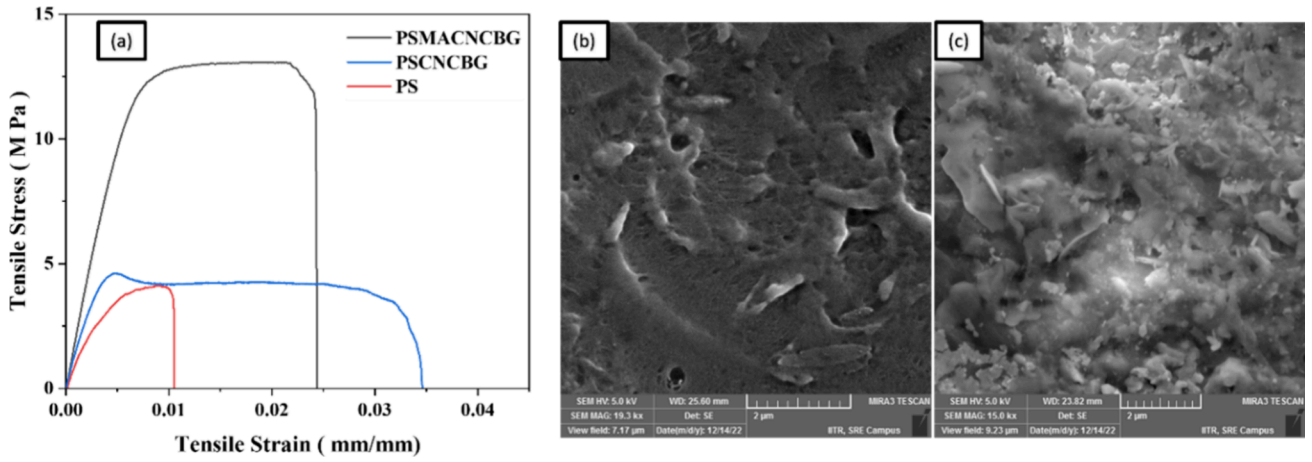

Figure 6. (a) Stress−strain curves of PS, PSCNCBG, and PSMACNCBG, and the surface morphological images of the composite films (b) PSCNCBG and (c) PSMACNCBG after tensile analysis.

signal in PS at 284.7, 285.5, and 291.7 eV correspond to the binding energies of aromatic C−C linkage, aliphatic C−C linkage, and C−C transition, respectively.[49,50] Additionally, the appearance of a new peak in PSCNCBG at 286.7 eV ascribes to the presence of C−O linkages of CNCBG. Furthermore, PSMACNCBG displayed all four distinct peaks attributed to PS and cellulose with a chemical shift in binding energies, and a new broad signal at 291 eV corresponds to the ester/acid linkages of the maleic anhydride group.[50] There is a significant shift in the aliphatic C−C linkage binding energy in PSMACNCBG compared to PS, i.e., from 285.5 to 286.1 eV. Similarly, the O 1s spectra were deconvoluted as shown in Figure S7a−c with binding energies at 531 and 532.5 eV corresponding to the oxygen of C−O/C−O-C, C═O from the CNCBG, MACNCBG.[51,52]

The shift in the binding energy can be attributed to introduced electron-withdrawing groups (ester and acid of MACNCBG). In general, the shift in the binding energies of electrons is governed by either electronic or chemical effects. In the case of PSMACNCBG, from the plausible reaction mechanism (Figure S5), it can be inferred that the presence of the electron-withdrawing group (−COOR/-COOH) is at the beta position from the reactive benzal carbon. This confirms that MACNCBG has formed a chemical bond with styrene monomer during in situ polymerization.

4.2.3. Mechanical Properties. This study's primary objective is to investigate the utilization of reactive filler during in situ polymerization. To improve the mechanical properties of PS 3 wt % of CNCBG, MACNCBG was used during the in situ polymerization of styrene. The mechanical properties of the PS, PSCNCBG, and PSMACNCBG films are evaluated, and the tensile-strain curve is represented in Figure 6a. The ultimate tensile strength of the PS, PSCNCBG (3 wt %) & PSMACNCBG (3 wt %) are 4.4 ± 0.20 MPa, 5.14 ± 0.45 MPa, and 13.1 ± 0.04 MPa, respectively. PS synthesized has demonstrated a lower tensile strength than the available commercial-grade polystyrene, as shown in Figure S8.

Although CNCBG has a comparable improvement in the ultimate tensile strength value, approximately 1.6 times higher than the PS; however, with MACNCBG, the enhancement was remarkable, with about 3.0 times higher in tensile strength, alongside imparting a semiductile behavior to the PS and at the same time improving the modulus as well. The chemical addition of MACNCBG at the benzal carbon of PS caused an excellent improvement in mechanical properties. However, PSMACNCBG (5 wt %) demonstrated a premature failure with the ultimate tensile strength of 3.4 ± 0.6 MPa, shown in Figure S6b.

It is not uncommon to expect such behavior with nanocellulose and its derivatives. The higher concentration of the CNCs and modified CNCs (5 wt %) often results in self-aggregation, eventually leading to a microseparation in the matrix. Other published literature reported a similar decline in the mechanical properties of the hydrophobic matrix during the incorporation of nanocellulose and its derivatives.[11,33,37,41]

Researchers employed MACNCs to improve the mechanical properties of PLA and epoxidized natural rubber. Somseemee et al. and Zhou et al. prepared the nanocomposites by adding MACNCs to an already synthesized polymer matrix, which improved their tensile strength by 1.08 and 2.26 times higher. However, the literature on utilizing modified nano cellulose as a reinforcer during in situ polymerization is very limited. The in situ polymerization exceptionally enhanced the tensile strength of PSMACNCBG (3.0 times higher) compared to the PS. FTIR and the tensile analysis showed that the 3 wt % MACNCBG employed was a reactive reinforcer, while the higher loading (5 wt %) resulted in the composite's phase separation and premature failure.

4.2.4. Surface Morphological Analysis. The FESEM images of PSCNCBG and PSMACNCBG are shown in Figure 6b, c. PSCNCBG shows physically entangled agglomerated CNCBG in the matrix, and PSMACNCBG displayed a chemically modified surface with a few unreacted MACNCBG nanorods. The explanation for such changes can be supported by inspecting the polymerization pathway. During stage-1 of PSCNCBG in situ emulsion polymerization, the styrene particles are stabilized in the micelle. Because of the hydrophilic head, the micelle could not allow the CNCBG to interact with the hydrophobic styrene monomer, eventually leading to physical entanglement with the PS after the polymerization. The higher crystallinity index of CNCBG nanorods and the physical interaction between the PS and CNCBG support improved mechanical properties despite its low suspension stability. Unlike PS and PSCNCBG, with two kinds of either empty or entrapped styrene micelles, PSMACNCBG led to a possible exclusive case of MACNCBG being inside the micelle during polymerization because of its modification, allowing it to interact with the styrene monomer.

https://doi.org/10.1021/acsomega.3c07849
ACS Omega 2024, 9, 33386−33396

Thus, supporting 3.0 wt % MACNCBG to exhibit this characteristic chemical behavior. The photographs of the prepared composite films are shown in Figure S9.

5. CONCLUSIONS

The current scientific investigation reports the synthesis of maleic anhydride-modified CNCs and their reactive reinforcing ability during the in situ polymerization of styrene. The CNCBG was successfully extracted from *Lagenaria siceraria* peels using 4 N HCl, unlike traditional H_2SO_4, and modified by maleic anhydride to produce MACNCBG with a yield of 90%. Both CNCBG and MACNCBG were characterized to evaluate the chemical structural changes involved. FTIR and ss NMR corroborated the successful grafting of maleic anhydride onto CNCBG. The modification improved the suspension stability of MACNCBG, leading to lower dimensional nanorods than CNCBG. The narrow-dimensional 3 wt % MACNCBG was utilized as a reactive filler during the in situ polymerization, and the PSMACNCBG composite was further characterized. The FTIR-spectra deconvolution of 2900−2800 cm^{-1} of PSMANCBG showed a new peak attributed to the C−H stretching of the bond formed between the benzal carbon of PS and the C=C bond of MACNCBG. PSCNCBG (3 wt %) and PSMACNCBG (3 wt %) exhibited improved mechanical properties, which are 1.2 and 3 times higher than PS. The utilization of MACNCBG during in situ polymerization can be further explored for an application-based advancement. With these improved mechanical properties, the composite PSMACNCBG has opened a pathway to incorporate reactive fillers during the in situ processes. This can be easily implemented with the existing commercial technology for sustainable and high-end engineering applications.

■ ASSOCIATED CONTENT

Supporting Information

The Supporting Information is available free of charge at https://pubs.acs.org/doi/10.1021/acsomega.3c07849.

Schematic representation of in situ emulsion polymerization; inhibitor removal process; comprehensive FTIR discussion of filler and composite; C.I. calculation from XRD via different methods; atomic weights percentage of the composites; TGA profile of MACNCBG; CNCs extracted from H_2SO_4 and HCl; FTIR of styrene and polystyrene; plausible reaction mechanism of PSMACNCBG; XPS O 1s deconvolution spectra of PS, PSCNCBG, PSMACNCBG; FTIR and tensile curve for 5 wt % composite; tensile comparison of synthesized PS with commercial PS; and photographs of prepared composite films (PDF)

■ AUTHOR INFORMATION

Corresponding Author

Pradip K. Maji − *Department of Polymer and Process Engineering, Indian Institute of Technology Roorkee, Saharanpur 240071, India;* orcid.org/0000-0001-8112-554X; Phone: +91-7895965010; Email: pradip@pe.iitr.ac.in

Authors

Radheesh Sharma Meda − *Department of Polymer and Process Engineering, Indian Institute of Technology Roorkee, Saharanpur 240071, India; Department of Chemical Engineering, Indian Institute of Technology Roorkee, Roorkee 247667, India;* orcid.org/0000-0001-7361-743X

Somya Jain − *Department of Polymer and Process Engineering, Indian Institute of Technology Roorkee, Saharanpur 240071, India; Department of Chemical Engineering, Indian Institute of Technology Roorkee, Roorkee 247667, India*

Shiva Singh − *Department of Polymer and Process Engineering, Indian Institute of Technology Roorkee, Saharanpur 240071, India;* orcid.org/0000-0003-4791-2587

Dakuri Ramakanth − *Department of Polymer and Process Engineering, Indian Institute of Technology Roorkee, Saharanpur 240071, India;* orcid.org/0000-0002-6463-231X

Shakshi Bhardwaj − *Department of Polymer and Process Engineering, Indian Institute of Technology Roorkee, Saharanpur 240071, India;* orcid.org/0000-0002-0539-4358

Yoshikuni Teramoto − *Division of Forest & Biomaterials Science, Graduate School of Agriculture, Kyoto University, Kyoto 6068502, Japan;* orcid.org/0000-0003-3850-3570

Prasenjit Mondal − *Department of Chemical Engineering, Indian Institute of Technology Roorkee, Roorkee 247667, India;* orcid.org/0000-0002-3101-9017

Complete contact information is available at: https://pubs.acs.org/10.1021/acsomega.3c07849

Notes

The authors declare no competing financial interest.

■ ACKNOWLEDGMENTS

The Science and Engineering Research Board, Govt of India, has supported this research project under grant no. (CRG/2021/004515). The authors, Shiva Singh and Shakshi Bharadwaj, gratefully acknowledge the Prime Minister Research Fellowship Program, Government of India, for financial support.

■ ABBREVIATIONS

CNCBG	cellulose nanocrystals extracted from bottle gourd peels
MA	maleic anhydride
MACNCBG	maleic anhydride-modified CNCBG
PS	polystyrene
PSCNCBG	cellulose nanocrystals reinforced polystyrene
PSMACNCBG	maleic anhydride-modified cellulose nanocrystals reinforced polystyrene

■ REFERENCES

(1) Gunko, V. M. Polymer Composites With Functionalized Silica. In *Polymer Composites with Functionalized Nanoparticles: Synthesis Properties, and Applications*; Elsevier, 2019; pp 119−148.

(2) Bansod, N. D.; Kapgate, B. P.; Maji, P. K.; Bandyopadhyay, A.; Das, C. FUNCTIONALIZATION OF EPDM RUBBER TOWARD BETTER SILICA DISPERSION AND REINFORCEMENT. *Rubber Chem. Technol.* **2019**, *92* (2), 219−236.

(3) Das, C.; Bansod, N. D.; Kapgate, B. P.; Rajkumar, K.; Das, A. Incorporation of Titania Nanoparticles in Elastomer Matrix to Develop Highly Reinforced Multifunctional Solution Styrene Butadiene Rubber Composites. *Polymer (Guildf)* **2019**, *162*, 1−10.

(4) Wajge, S. W.; Das, C. Generating Crosslinking Network in XNBR Based on Copper (I)−Carboxylate Interaction. *Polym. Adv. Technol.* **2023**, *34* (3), 998−1007.

(5) Oğuz, O.; Monfared Zanjani, J. S.; Soytaş, S. H.; Menceloğlu, Y. Z. Specific Interactions and Self-Organization in Polymer/Functionalized Nanoparticle Systems. *Polymer Composites with Functionalized Nanoparticles* **2019**, 85−117.
(6) Roy, K.; Mandal, S. K.; Alam, M. N.; Debnath, S. C. A Comparison between Polyethylene Glycol (PEG) and Polypropylene Glycol (PPG) Treatment on the Properties of Nano-Titanium Dioxide (TiO2) Based Natural Rubber (NR) Nanocomposites. *Polym. Bull.* **2016**, *73* (11), 3065−3079.
(7) Ambilkar, S. C.; Das, C. Surface Modification of Zirconia by Various Modifiers to Investigate Its Reinforcing Efficiency toward Nitrile Rubber. *Polym. Compos* **2023**, *44* (3), 1512−1521.
(8) Rosli, N. A.; Ahmad, I.; Anuar, F. H.; Abdullah, I. Effectiveness of Cellulosic Agave Angustifolia Fibres on the Performance of Compatibilised Poly(Lactic Acid)-Natural Rubber Blends. *Cellulose* **2019**, *26* (5), 3205−3218.
(9) Han, J.; Lu, K.; Yue, Y.; Mei, C.; Huang, C.; Wu, Q.; Xu, X. Nanocellulose-Templated Assembly of Polyaniline in Natural Rubber-Based Hybrid Elastomers toward Flexible Electronic Conductors. *Ind. Crops Prod* **2019**, *128*, 94−107.
(10) Xiong, X. Q.; Bao, Y. L.; Liu, H.; Zhu, Q.; Lu, R.; Miyakoshi, T. Study on Mechanical and Electrical Properties of Cellulose Nanofibrils/Graphene-Modified Natural Rubber. *Mater. Chem. Phys.* **2019**, *223*, 535−541.
(11) Singh, S.; Dhakar, G. L.; Kapgate, B. P.; Maji, P. K.; Verma, C.; Chhajed, M.; Rajkumar, K.; Das, C. Synthesis and Chemical Modification of Crystalline Nanocellulose to Reinforce Natural Rubber Composites. *Polym. Adv. Technol.* **2020**, *31* (12), 3059−3069.
(12) Patil, S. P.; Shendye, P.; Markert, B. Molecular Dynamics Simulations of Silica Aerogel Nanocomposites Reinforced by Glass Fibers, Graphene Sheets and Carbon Nanotubes: A Comparison Study on Mechanical Properties. *Compos B Eng.* **2020**, *190*, No. 107884.
(13) Merino, D.; Gutiérrez, T. J.; Mansilla, A. Y.; Casalongué, C. A.; Alvarez, V. A. Critical Evaluation of Starch-Based Antibacterial Nanocomposites as Agricultural Mulch Films: Study on Their Interactions with Water and Light. *ACS Sustain Chem. Eng.* **2018**, *6* (11), 15662−15672.
(14) Bos, H. L.; Müssig, J.; van den Oever, M. J. A. Mechanical Properties of Short-Flax-Fibre Reinforced Compounds. *Compos Part A Appl. Sci. Manuf* **2006**, *37* (10), 1591−1604.
(15) Soleimani, E.; Zamani, N. Surface Modification of Alumina Nanoparticles: A Dispersion Study in Organic Media. *Acta Chim Slov* **2017**, *64* (3), 644−653.
(16) Meda, R. S.; Jain, S.; Singh, S.; Verma, C.; Nandi, U.; Maji, P. K. Novel Lagenaria Siceraria Peel Waste Based Cellulose Nanocrystals: Isolation and Rationalizing H-Bonding Interactions. *Ind. Crops Prod* **2022**, *186*, No. 115197.
(17) Bhardwaj, S.; Singh, S.; Meda, R. S.; Jain, S.; Maji, P. K. Structural and Morphological Exploration of Cellulose Nanocrystals Extracted from Lignocellulosic Waste Biomass of Brassica Nigra (Mustard Straw). *Biomass Convers. Biorefin.* **2023**, *1*, 1−14.
(18) Gupta, P.; Pandey, A.; Gaikwad, K. K.; Roy, S.; Maji, P. K. The Role of Rheological Premonitory of Hydrogels Based on Cellulose Nanofibers and Polymethylsilsesquioxane on the Physical Properties of Corresponding Aerogels. *Polym. Eng. Sci.* **2021**, *61* (4), 1220−1231.
(19) Verma, C.; Chhajed, M.; Singh, S.; Sathwane, M.; Maji, P. K. Bioinspired Structural Color Sensors Based on Self-Assembled Cellulose Nanocrystal/Citric Acid to Distinguish Organic Solvents. *Colloids Surf., A* **2022**, *655*, No. 130206.
(20) Chhajed, M.; Verma, C.; Sathawane, M.; Singh, S.; Maji, P. K. Mechanically Durable Green Aerogel Composite Based on Agricultural Lignocellulosic Residue for Organic Liquids/Oil Sorption. *Mar. Pollut. Bull.* **2022**, *180*, No. 113790.
(21) Lu, P.; Hsieh, Y. Lo. Preparation and Properties of Cellulose Nanocrystals: Rods, Spheres, and Network. *Carbohydr. Polym.* **2010**, *82* (2), 329−336.
(22) Kobe, R.; Iwamoto, S.; Endo, T.; Yoshitani, K.; Teramoto, Y. Stretchable Composite Hydrogels Incorporating Modified Cellulose Nanofiber with Dispersibility and Polymerizability: Mechanical Property Control and Nanofiber Orientation. *Polymer (Guildf)* **2016**, *97*, 480−486.
(23) Chakrabarty, A.; Teramoto, Y. Recent Advances in Nanocellulose Composites with Polymers: A Guide for Choosing Partners and How to Incorporate Them. *Polymers* **2018**, *10* (5), 517.
(24) Pu, Y.; Zhang, J.; Elder, T.; Deng, Y.; Gatenholm, P.; Ragauskas, A. J. Investigation into Nanocellulosics versus Acacia Reinforced Acrylic Films. *Composites, Part B* **2007**, *38*, 360−366, DOI: 10.1016/j.compositesb.2006.07.008.
(25) Roohani, M.; Habibi, Y.; Belgacem, N. M.; Ebrahim, G.; Karimi, A. N.; Dufresne, A. Cellulose Whiskers Reinforced Polyvinyl Alcohol Copolymers Nanocomposites. *Eur. Polym. J.* **2008**, *44* (8), 2489−2498.
(26) Cao, X.; Dong, H.; Li, C. M. New Nanocomposite Materials Reinforced with Flax Cellulose Nanocrystals in Waterborne Polyurethane. *Biomacromolecules* **2007**, *8* (3), 899−904.
(27) Junior de Menezes, A.; Siqueira, G.; Curvelo, A. A. S.; Dufresne, A. Extrusion and Characterization of Functionalized Cellulose Whiskers Reinforced Polyethylene Nanocomposites. *Polymer (Guildf)* **2009**, *50* (19), 4552−4563.
(28) Durán, N.; Lemes, A. P.; Durán, M.; Freer, J.; Baeza, J. A minireview of cellulose nanocrystals and its potential integration as co-product in bioethanol production. *J. Chil. Chem. Soc.* **2011**, *56* (2), 672−677, DOI: 10.4067/S0717-97072011000200011.
(29) Iwamoto, S.; Endo, T. 3 Nm Thick Lignocellulose Nano Fibers Obtained from Esterified Wood with Maleic Anhydride. *ACS Macro Lett.* **2015**, *4* (1), 80−83.
(30) Singh, S.; Bhardwaj, S.; Meda, R. S.; Verma, C.; Chhajed, M.; Ghosh, K.; Maji, P. K. Insights into Thermal Degradation Kinetics and Liquid Crystalline Behavior of Cellulose Nanocrystals from the Waste of Cajanus Cajan (Pigeon Pea). *Int. J. Biol. Macromol.* **2023**, *242*, No. 124507.
(31) Yu, H.; Qin, Z.; Liang, B.; Liu, N.; Zhou, Z.; Chen, L. Facile Extraction of Thermally Stable Cellulose Nanocrystals with a High Yield of 93% through Hydrochloric Acid Hydrolysis under Hydrothermal Conditions. *J. Mater. Chem. A Mater.* **2013**, *1* (12), 3938−3944.
(32) Araki, J.; Wada, M.; Kuga, S.; Okano, T. Flow Properties of Microcrystalline Cellulose Suspension Prepared by Acid Treatment of Native Cellulose. *Colloids Surf. A Physicochem Eng. Asp* **1998**, *142* (1), 75−82.
(33) Zhou, L.; He, H.; Li, M. C.; Huang, S.; Mei, C.; Wu, Q. Enhancing Mechanical Properties of Poly(Lactic Acid) through Its in-Situ Crosslinking with Maleic Anhydride-Modified Cellulose Nanocrystals from Cottonseed Hulls. *Ind. Crops Prod.* **2018**, *112*, 449−459.
(34) Ramakanth, D.; Singh, S.; Bhardwaj, S.; Meda, R. S.; Gaikwad, K. K.; Maji, P. K. Green Synthesis and Characterization of Polymyrcene as an Oxygen Scavenging Sustainable Polymer for Active Food Packaging Applications. *ACS Appl. Polym. Mater.* **2023**, *5* (12), 9888−9897.
(35) Park, S.; Baker, J. O.; Himmel, M. E.; Parilla, P. A.; Johnson, D. K. Cellulose Crystallinity Index: Measurement Techniques and Their Impact on Interpreting Cellulase Performance. *Biotechnol. Biofuels Bioprod.* **2010**, *3* (1), 10.
(36) Sclavons, M.; Franquinet, P.; Carlier, V.; Verfaillie, G.; Fallais, I.; Legras, R.; Laurent, M.; Thyrion, F. C. Quantification of the Maleic Anhydride Grafted onto Polypropylene by Chemical and Viscosimetric Titrations, and FTIR Spectroscopy. *Polymer (Guildf)* **2000**, *41* (6), 1989−1999.
(37) Wu, C.; Zhang, X.; Wang, X.; Gao, Q.; Li, X. Surface Modification of Cellulose Nanocrystal Using Succinic Anhydride and Its Effects on Poly(Butylene Succinate) Based Composites. *Cellulose* **2019**, *26* (5), 3167−3181.
(38) Wikberg, H.; Maunu, S. L. Characterisation of Thermally Modified Hard- and Softwoods by 13C CPMAS NMR. *Carbohydr. Polym.* **2004**, *58* (4), 461−466.

https://doi.org/10.1021/acsomega.3c07849
ACS Omega 2024, 9, 33386−33396

(39) Yu, X.; Tong, S.; Ge, M.; Wu, L.; Zuo, J.; Cao, C.; Song, W. Adsorption of Heavy Metal Ions from Aqueous Solution by Carboxylated Cellulose Nanocrystals. *Journal of Environmental Sciences* **2013**, *25* (5), 933−943.
(40) Vivian Abiaziem, C.; Bassey Williams, A.; Ibijoke Inegbenebor, A.; Theresa Onwordi, C.; Ehi-Eromosele, C. O.; Felicia Petrik, L. Preparation and Characterisation of Cellulose Nanocrystal from Sugarcane Peels by XRD, SEM and CP/MAS 13C NMR. *J. Phys.: Conf. Ser.* **2019**, *1299* (1), No. 012123.
(41) Somseemee, O.; Saeoui, P.; Schevenels, F. T.; Siriwong, C. Enhanced Interfacial Interaction between Modified Cellulose Nanocrystals and Epoxidized Natural Rubber via Ultraviolet Irradiation. *Sci. Rep.* **2022**, *12* (1), 1−13.
(42) Princi, E.; Vicini, S.; Proietti, N.; Capitani, D. Grafting Polymerization on Cellulose Based Textiles: A 13C Solid State NMR Characterization. *Eur. Polym. J.* **2005**, *41* (6), 1196−1203.
(43) Singh, S.; Bhardwaj, S.; Verma, C.; Chhajed, M.; Balayan, K.; Ghosh, K.; Maji, P. K. Elliptically Birefringent Chemically Tuned Liquid Crystalline Nanocellulose Composites for Photonic Applications. *J. Mol. Liq.* **2022**, *366*, No. 120326.
(44) Cheng, M.; Qin, Z.; Chen, Y.; Hu, S.; Ren, Z.; Zhu, M. Efficient Extraction of Cellulose Nanocrystals through Hydrochloric Acid Hydrolysis Catalyzed by Inorganic Chlorides under Hydrothermal Conditions. *ACS Sustainable Chem. Eng.* **2017**, *5* (6), 4656−4664.
(45) Zhou, Y.; Jin, Q.; Hu, X.; Zhang, Q.; Ma, T. Heavy Metal Ions and Organic Dyes Removal from Water by Cellulose Modified with Maleic Anhydride. *J. Mater. Sci.* **2012**, *47* (12), 5019−5029.
(46) Martínez, F.; Uribe; Andrés, E.; Olea, F. F. Copolymerization of Maleic Anhydride with Styrene and α-Olefins. Molecular and Thermal Characterization. *J. Macromol. Sci., Part A: Pure Appl.Chem.* **2005**, *42* (8), 1063−1072.
(47) Zuo, Y.; Gu, J.; Yang, L.; Qiao, Z.; Tan, H.; Zhang, Y. Synthesis and Characterization of Maleic Anhydride Esterified Corn Starch by the Dry Method. *Int. J. Biol. Macromol.* **2013**, *62*, 241−247.
(48) Samadi, N.; Ansari, R.; Khodavirdilo, B. Removal of Copper Ions from Aqueous Solutions Using Polymer Derivations of Poly (Styrene-Alt-Maleic Anhydride). *Egyptian Journal of Petroleum* **2017**, *26* (2), 375−389.
(49) Girardeaux, C.; Pireaux, J.-J. Analysis of Polystyrene (PS) by XPS. *Surface Science Spectra* **1996**, *4* (2), 130−133.
(50) Goodson, M. L.; Lagle, R.; Guggilla, P. X-Ray Photoelectron Spectroscopy of Polystyrene Composite Films. *Journal of Advanced Materials Science and Engineering* **2022**, *2* (1), 4−8.
(51) Abdellah, M. H.; Pérez-Manríquez, L.; Puspasari, T.; Scholes, C. A.; Kentish, S. E.; Peinemann, K. V. Effective Interfacially Polymerized Polyester Solvent Resistant Nanofiltration Membrane from Bioderived Materials. *Adv. Sustain Syst* **2018**, *2* (7), No. 1800043.
(52) Liu, Y.; Hu, J. Investigation of Polystyrene-Based Microspheres from Different Copolymers and Their Structural Color Coatings on Wood Surface. *Coatings* **2021**, *11* (1), 1−14.

https://doi.org/10.1021/acsomega.3c07849
ACS Omega 2024, 9, 33386−33396